Improved Precipitation Typing Using POSS Spectral Modal Analysis

BRIAN E. SHEPPARD,[a] MERHALA THURAI,[b] PETER RODRIGUEZ,[a] PATRICK C. KENNEDY,[c] AND DAVID R. HUDAK[a]

[a] *Meteorological Research Division, Environment and Climate Change Canada, Toronto, Ontario, Canada*
[b] *Department of Electrical and Computer Engineering, Colorado State University, Fort Collins, Colorado*
[c] *Department of Atmospheric Science, Colorado State University, Fort Collins, Colorado*

(Manuscript received 5 June 2020, in final form 21 October 2020)

ABSTRACT: The Precipitation Occurrence Sensor System (POSS) is a small X-band Doppler radar that measures the Doppler velocity spectra from precipitation falling in a small volume near the sensor. The sensor records a 2D frequency of occurrence matrix of the velocity and power at the mode of each spectrum measured over 1 min. The centroid of the distribution of these modes, along with other spectral parameters, defines a data vector input to a multiple discriminant analysis (MDA) for classification of the precipitation type. This requires the a priori determination of a training set for different types, particle size distributions (PSDs), and wind speed conditions. A software model combines POSS system parameters, a particle scattering cross section, and terminal velocity models, to simulate the real-time Doppler signal measured by the system for different PSDs and wind speeds. This is processed in the same manner as the system hardware to produce bootstrap samples of the modal centroid distributions for the MDA training set. MDA results are compared to images from the Multi-Angle Snowflake Camera (MASC) at the MASCRAD site near Easton, Colorado, and to the CSU–CHILL X-band radar observations from Greeley, Colorado. In the four case studies presented, POSS successfully identified precipitation transitions through a range of types (rain, graupel, rimed dendrites, aggregates, unrimed dendrites). Also two separate events of hail were reported and confirmed by the images.

KEYWORDS: Precipitation; Remote sensing; Surface observations; Classification; Automatic weather stations; Spectral analysis/models/distribution

1. Introduction

Environment and Climate Change Canada (ECCC) began automating its surface weather-observing network over a period of several decades starting in the late 1960s. In 1988 the new generation of autostation included for the first time a prototype Precipitation Occurrence Sensor System (POSS) in its suite of sensors. The instrument consists of a small continuous wave bistatic X-band Doppler radar and a signal processor unit, both designed and developed in-house. This system measures 1-min average Doppler velocity spectra of precipitation particles traversing a small volume near the surface. As its name suggests it was initially intended to report only the occurrence of precipitation but analysis of the spectrum can distinguish liquid from solid and its intensity. The initial design was licensed to commercial manufacturers for approximately 200 systems to meet the needs of the expanding Canadian national Automated Weather Observing System (AWOS) network. Apart from this operational requirement, POSS can estimate liquid raindrop size distributions (a disdrometer), e.g., Campos and Zawadzki (2000) and Chang et al. (2020), and radar reflectivity and liquid water equivalent rates in solid precipitation, e.g., Huang et al. (2015). It has been a valuable component of several research field experiments, e.g., Global Precipitation Measurement Cold Season Precipitation Experiment (GCPEX) (Skofronick-Jackson et al. 2015), as part of the Global Precipitation Measurement (GPM) mission ground validation activities, and Integrated Characterization of Energy, Clouds, Atmospheric State, and Precipitation at Summit (ICECAPS) (Pettersen et al. 2018). It has been used to support studies on the parameterization of microphysical processes and numerical models, e.g., Szyrmer and Zawadzki (2010). ECCC continues to support many field campaigns with the loan and operation of POSS, as well as data analysis. This paper presents for the first time a new technique for using POSS data to classify precipitation type.

POSS has several advantages over other methods of precipitation classification where surface measurements are needed to validate satellite-based observations. Surface-based disdrometers and precipitation classification sensors typically have measurement volumes several orders of magnitude smaller than POSS. This can result in missing low number concentrations of hailstones, for example. Unlike conventional and space-based radars, the POSS measurement is at the surface. Vertical winds above the surface will affect terminal velocity measurements made by larger vertical-pointing Doppler radars. Vertical winds in the POSS measurement volume are low. Large horizontal winds affect the POSS measurement especially when used as a disdrometer.

Compared to conventional catchment gauges POSS is better able to measure light precipitation. This is especially true for solid precipitation, which is vulnerable to gauge losses due to several causes: wetting, evaporation, wind, see chapter 6.4 of the World Meteorological Organization Guide to Meteorological

---

Denotes content that is immediately available upon publication as open access.

Supplemental information related to this paper is available at the Journals Online website: https://doi.org/10.1175/JTECH-D-20-0075.s1.

Corresponding author: Peter Rodriguez, peter.rodriguez@ec.gc.ca

DOI: 10.1175/JTECH-D-20-0075.1

Instruments and Methods of Observation (the CIMO Guide) (WMO 2018). This capability is important in climates where long periods of very light snow may result in significant accumulation that is missed by conventional gauges (Pettersen et al. 2018).

Optical sensors that image or measure scattering by solid particles have difficulty determining their water content because their primary response is to the physical size of the particle. For radars like POSS scattering by solid particles meeting the Rayleigh criteria will depend only on the square of their mass. Also, in general, optical sensors require more field maintenance to keep optics clean and aligned.

This paper presents an analysis technique to better distinguish precipitation types, particularly for solid precipitation, by using the POSS Doppler spectral modal data. Historically, for the automated weather station application, the modal velocity of the 1-min average Doppler spectrum (i.e., velocity of the maximum spectral power component) has been used to estimate precipitation type. However, the POSS also records the modal power and velocity of the individual Doppler spectra used in the 1-min average. These data are collected routinely as part of all field experiments but have not previously been analyzed.

The paper is organized as follows. In section 2, the POSS instrument and signal processing are described. Section 3 describes the model components required for the forward simulation of the POSS Doppler spectrum. Section 4 explains the Doppler spectral modal frequency of occurrence matrix and plots. Section 5 explores the effect of various factors on the modal centroid distributions. Section 6 presents the multiple discriminant analysis (MDA) of the centroid distributions for the identification of type. Section 7 gives several case studies comparing POSS precipitation classification to collocated images of precipitation particles made by the Multi-Angle Snowflake Camera (MASC; Garrett et al. 2012) in 2015–16. The instruments were collocated at a test site in Easton, Colorado, as part of the MASCRAD (MASC+Radar) field experiment (Notaroš et al. 2016). The events were chosen in part because they represented interesting transitions in type as well as including some hail occurrences. Section 8 discusses the Colorado State University–University of Chicago–Illinois State Water Survey (CSU–CHILL) dual-polarization radar data during the four POSS classification cases. Last, section 9 gives the conclusions.

2. Instrument description and signal processing

The POSS is a small bistatic, continuous wave (CW), horizontally polarized, X-band (10.5 GHz) Doppler radar (Sheppard 1990, hereafter S1990). The central axes of the transmitter and receiver beams intersect at about 34 cm above the antenna radomes and the maximum power is received from a location 28 cm above the radomes, referred to hereafter as the "hot spot." Because POSS is a CW radar, the measurement volume is not defined by range gating, but rather by the distance at which the scattered signal amplitude falls below the detection threshold of the system. The amplitude depends on the combined antenna pattern of the transmitter and receiver, the distance to the scatterer, and the scattering cross section at the bistatic scattering angle. For example, the largest raindrops (~6 mm) are detected to a maximum height of 3 m above the radomes and from a total volume of about 34 m^3.

The POSS signal processing is described in more detail in S1990 and Table 1 of Sheppard (2007, hereafter S2007). POSS digitizes the Doppler voltage output from the radar receiver sensor head at 2.048 kHz rate. A power density spectrum of 128 analog to digital samples is calculated by fast Fourier transform. Depending on the version of POSS hardware, about 380 or 960 spectra are averaged over 1-min before output. The spectral frequency resolution of 16 Hz corresponds to a Doppler velocity resolution of about 0.223 $m\,s^{-1}$.

3. Simulated Doppler velocity spectra

It is necessary to forward model the POSS measurement to calibrate the system for any habit, particle size distribution (PSD) and wind condition. For each particle size, the Doppler power and frequency are dependent on its location and velocity in the measurement volume (S2007, his Fig. 2). Because in real time the location is unknown, the simulation is based on random sampling of the population of signals generated from locations in a cube with horizontal cross-sectional dimensions from -200 to $+200$ cm and vertical dimension from -15 to 200 cm.

The simulation here differs from earlier work (S1990). Previously, a volume-averaged Doppler spectrum was determined for the specified particle size associated with each measurement channel. A composite Doppler velocity spectrum was generated by summing in the frequency domain these volume-averaged Doppler spectra weighted by the number of particles in each measurement channel.

In the present work, the composite "raw" Doppler signal is simulated in the time domain by summation of the Doppler voltages simultaneously produced from all the particle sizes in the measurement volume. Thus, the real-time POSS processing algorithms operating on the raw Doppler voltage can be more realistically simulated.

The radar system constants are determined from laboratory measurements of the Doppler signal from a water drop of known size (Sheppard and Joe 2008).

The simulation of the measured Doppler velocity spectrum requires three model components: a PSD (section 3a), a terminal velocity (section 3b), and a scattering cross section (section 3c). The simulation steps are described in appendix B.

Each of the three model components uses a different parameter to describe the particle size and care must be taken when combining the models and also when applying literature research. The liquid and solid, with the exception of hail, PSDs models used here are given as functions of the diameter of a liquid water sphere of equivalent mass (D_m). For terminal velocity formulations it is common to use the maximum dimension in three dimensions ($D_{\max}$). Sometimes $D_{\max}$ is defined as the maximum dimension of the particle's projection normal to the direction of fall, which is not necessarily equal to the maximum dimension in three dimensions, as noted by Heymsfield and Westbrook (2010, hereafter HW2010). The significance of this difference has not been evaluated here.

Scattering cross-section calculations commonly use the diameter of a sphere (D_s) with volume equivalent to that of the particle.

The relationship between these three different size parameters for a particle of mass m is

$$m = \frac{\pi}{6}\rho_l D_m^3 = \frac{\pi}{6}\rho_b D_{\max}^3 = \frac{\pi}{6}\rho_v D_s^3, \tag{1}$$

where ρ_l is the density of liquid water (assumed 1 g cm^{-3}), ρ_b is referred to as the "bulk" density, and ρ_v as the "volumetric" density. As noted by Heymsfield and Wright (2014, hereafter HW2014), ρ_b defined in this way includes two sources of the reduction in density of an ice–air mixture. First, the spherical volume of diameter $D_{\max}$ enveloping a nonspherical shape contains air external to the particle. Second, there may also be air embedded in the particle. Note that ρ_v is only affected by the embedded air and $\rho_v > \rho_b$, with the equality only applying to spherical particles.

It is convenient to use D_m to define the POSS measurement channels. Because D_m is the size parameter most commonly used in defining PSD models it simplifies the integration of bulk parameters such as precipitation rate over the measurement channels. Also at X-band frequencies the power received from the hot spot is proportional to D_m^6, independent of ρ_v, for spherical particles of size $D_s \lesssim 2.5$ mm for liquid, and $D_s \lesssim 3.8$ mm for ice.

a. *Particle size distribution models*

For liquid precipitation the PSD uses the Marshall–Palmer (M-P) model (Marshall and Palmer 1948):

$$N(D_m) = N_0 e^{-\lambda D_m}, \tag{2}$$

where $N_0 = 8000$ m^{-3} mm^{-1}, $\lambda = 4.1R_{\mathrm{MP}}^{-0.21}$ mm^{-1}, and R_{MP} is referred to here as the "M-P model rate" (mm h^{-1}), which is a special case of the modified gamma distribution model, e.g., Ulbrich (1983):

$$N(D_m) = N_0 D_m^{\mu} e^{-\lambda D_m}, \tag{3}$$

with the exponent $\mu = 0$. The coefficient N_0 has units of m^{-3} mm$^{-1-\mu}$.

For all solid precipitation except hail, the PSD assumes the Sekhon–Srivastava (S-S) model (Sekhon and Srivastava 1970). This has the same exponential form as (2), but with $N_0 = 2500R_{\mathrm{SS}}^{-0.94}$ m^{-3} mm^{-1} and $\lambda = 2.29R_{\mathrm{SS}}^{-0.45}$ mm^{-1}, where R_{SS} is the model liquid equivalent rate (mm h^{-1}).

For hail, the PSD used here has the same form as (2) but with D_s instead of D_m. The coefficient N_0 is from Cheng et al. [1985, their Eq. (2)], $N_0 = 100\lambda^{4.11}$ m^{-3} mm^{-1}. The exponent λ has been derived for the first time here from measured data given in Cheng and English (1983). The precipitation rate values in their Table 1 were synchronized with λ values digitized from their Fig. 5 by assuming inverse proportionality. A linear regression of 35 observations gave $\lambda = 0.7R^{-0.4}$ mm^{-1}.

b. *Terminal velocity model*

The measured Doppler velocity v_{dop} (calm conditions) is always less than the terminal velocity v_t (S2007, his Fig. 2) because of the POSS bistatic scattering geometry. A particle traversing the hot spot with velocity v_t will produce v_{dop} given by

$$v_{\mathrm{dop}} \approx 0.91 v_t. \tag{4}$$

Table 1 presents ranges of particle sizes (D_m, $D_{\max}$, and D_s) and the corresponding range of v_t for each habit used in the simulations.

For raindrops, the D_m is determined from v_t using a regression equation given by Foote and Du Toit (1969) in their Table 1.

For solid types, $v_t = f(D_m)$ is determined following the approach of HW2010, which is an extension of the work of Mitchell (1996, hereafter M1996), given in appendix A. Mitchell formulated the mass (m) and area (A) projected to the flow as power-law expressions of $D_{\max}$:

$$m = \alpha D_{\max}^{\beta} \tag{5}$$

and

$$A = \gamma D_{\max}^{\sigma}, \tag{6}$$

where α, β, γ, and σ are referred to here as the Mitchell parameters and their values are given for the habits listed in Table 1.

A convenient means of determining the effect of riming on the Mitchell parameters was developed by Erfani and Mitchell (2017, hereafter EM2017). They concluded from ground-based measurements of m and $D_{\max}$ that β is constant during the riming process for dendrites. Fontaine et al. (2014) established a linear expression between β and σ implying that σ is also constant during riming. EM2017 assumed a linear relationship between A and m to calculate the effect of riming on γ in (6).

The HW2010 model uses a representation of the drag coefficient (C_d):

$$C_d = C_o\left(1 + \frac{\delta_0}{\sqrt{\mathrm{Re}}}\right)^2, \tag{7}$$

where the two dimensionless constants are C_o, the pressure drag coefficient, and δ_0, the surface roughness parameter. These are also given in Table 1. There has been some discussion in the literature, e.g., Khvorostyanov and Curry (2005), regarding the values of C_o and δ_0. HW2010 determined values ($C_o = 0.35$ and $\delta_0 = 8$) based on minimizing scatter in a plot (their Fig. 8) of the modified drag coefficient (C_d^*) [their Eq. (7)] and the Reynolds number (Re) for Re < 1000. These data, derived from a number of sources of experimental tank measurements, were primarily for planar-shaped particles. It did not include graupel or hail sized particles. Böhm (1989), M1996, and Mitchell and Heymsfield (2005, hereafter MH2005), used values of $C_o = 0.6$ and $\delta_0 = 5.83$. These values gave better agreement with v_t measurements for graupel, ice pellets and hail and were used for these habits here. The HW2010 values were used for all other solid types.

Terminal velocity is also dependent on air density. For the case studies given here, the POSS was located at a test site at

TABLE 1. Parameters for different hydrometeors used in POSS simulations.

	Rain	Unrimed dendrite	Aggregate	Rimed dendrite (R2b)	Lump graupel: < 0.1 g cm^{-3}	Lump graupel: 0.1–0.2 g cm^{-3}	Lump graupel: 0.2–0.45 g cm^{-3}	Ice pellets	Hail
v_t min (m s^{-1})[a]	1.23	0.12	0.37	0.49	0.49	0.49	0.49	0.73	8.83
v_t max (m s^{-1})	10.06	0.61	1.1	1.35	3.68	4.17	5.40	11.28	15.45
Eq. (13) ρ_v range (g cm^{-3})	1	0.028–0.92	0.096–0.92	0.054–0.92	0.158	0.189–0.353	0.261–0.810	0.91	0.89
D_m min (mm)	0.31	0.09	0.14	0.19	0.28	0.22	0.18	0.22	5.07
D_m max (mm)	7.16	1.46	3.17	3.31	3.66	4.08	5.29	7.72	13.89
$D_{\max}$ min (mm)	0.31	0.19	0.21	0.29	0.65	0.39	0.24	0.23	5.28
$D_{\max}$ max (mm)	9.03	19.0	38.85	35.5	8.48	8.91	10.37	7.97	14.44
D_S min (mm)	0.31	0.10	0.14	0.19	0.52	0.31	0.19	0.23	5.28
D_S max (mm)	7.16	4.79	6.58	16.9	6.76	7.11	8.28	7.97	14.44
Axial ratio of oblate spheroid	Eq. (8)	0.05	0.05[b]	0.5	1	1	1	1	1
Source of Mitchell[d] parameters	—	HK1987 [c]	MH2005	EM2017	LH1974	LH1974	LH1974	NF2015	M1996
α	—	6.12×10^{-4}	1.45×10^{-3}	1.988×10^{-3}	4.2×10^{-2}	4.914×10^{-2}	7.0168×10^{-2}	4.76×10^{-1}	4.66×10^{-1}
β	—	2.29	1.8	1.78	3	2.8	2.7	3	3
γ	—	0.32475	0.229	Function of riming	0.5	0.5	0.5	0.785	0.785
σ	—	2.0	1.88	1.45	2	2	2	2	2
C_o[e]	—	0.35[f]	0.35[f]	0.35[f]	0.6[g]	0.6[g]	0.6[g]	0.6[g]	0.6[g]
δ_0[e]	—	8[f]	8[f]	8[f]	5.83[g]	5.83[g]	5.83[g]	5.83[g]	5.83[g]
Scattering model[h]	T	DDA	DDA	T	T	T	T	DDA	DDA

[a] Velocities are for elevation, 1469 m MSL, at Easton, where air density is 0.001 061 g cm^{-3} as per International Standard Atmosphere (ISO 1975).

[b] Kajikawa (1972).

[c] Heymsfield and Kajikawa (1987).

[d] M1996 parameters [his Eqs. (15) and (16)] are in cgs units.

[e] C_0 (dimensionless) is the asymptotic value of the drag coefficient at large Reynolds number, and δ_0 (dimensionless) is the boundary layer parameter. See, e.g., (6) of HW2010.

[f] HW2010 fit to match tank measurements of primarily planar crystals.

[g] Böhm (1989) for ice particles according to MH2005 (p. 1638).

[h] T matrix (T) or discrete dipole approximation (DDA).

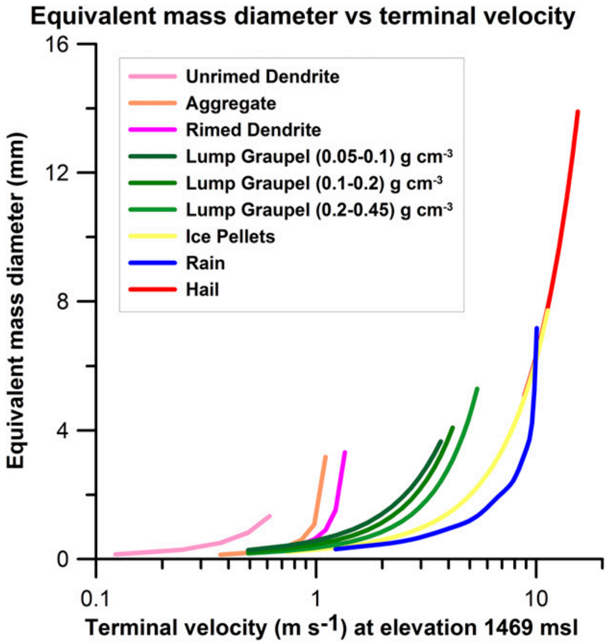

FIG. 1. Plot of equivalent mass diameter (D_m) as a function of terminal velocity (v_t) for several precipitation types.

Easton. For this elevation, 1469 m MSL, the air density based on the International Standard Atmosphere [International Organization for Standardization (ISO); ISO 1975] is 0.001 061 g cm^{-3}. Figure 1 shows the $D_m = f(v_t)$ for several habits.

c. Scattering cross-section model

The scattering cross section is calculated for each $D_m(j)$ corresponding to jth Doppler spectral component $v_{\mathrm{dop}}(j)$ for each habit. Two formulations are used: T matrix (Mishchenko 2000) and the discrete dipole approximation (DDA) (Draine and Flatau 1994). The DDA software DDSCAT version 7.3.1 (Draine and Flatau 2013) is available (http://ddscat.wikidot.com). The T-matrix approach can only be used with particles with rotational axial symmetry such as raindrops. Both models require specification of D_s, the complex refractive index m_r, and particle shape. Both models permit different orientations of the axis of rotation (canting angle). It is assumed to be zenith pointing for this analysis.

The shape of falling raindrops distorts from spheres due to aerodynamic effects. An oblate spheroid at terminal velocity is assumed with minor to major axial ratio (Brandes et al. 2002) given by

$$r = 0.9951 + 0.0250D_s - 0.036\,44D_s^2 + 0.005\,030D_s^3 - 0.000\,249\,2D_s^4, \tag{8}$$

where D_s is in mm.

Solid precipitation is also modeled as an oblate spheroid with axial ratio specified for each habit (Table 1).

The DDA model approximates the scatterer by an array of point dipoles (polarizable points). The scattering of an incident electromagnetic wave interacting with this array is then solved. The model is suitable for any shape and composition of scatterer if two conditions are met (Draine and Flatau 2013):

1) Size parameter $D_s/\lambda \le 25$, where λ is the radar wavelength; for POSS, $\lambda = 28.5$ mm, this condition is always met by any precipitation,
2) $|m_r - 1| \le 2$, where m_r is the complex refractive index; at X-band wavelengths this refractive index condition is only met for ice and not liquid water.

The dipole array coordinates and composition are either user specified or, for certain standard shapes, are supplied with the software. Table 1 indicates which model was used in the simulations for each habit.

1) REFRACTIVE INDEX

The complex refractive index m_r is determined as follows. For liquid water, m_r has real part $\Re(m_r) = 7.96$, and imaginary part $\Im(m_r) = 2.13$ (Ray 1972).

For ice, $\Re(m_r) = 1.78$ (Gunn and East 1954), and $\Im(m_r) = 1.123 \times 10^{-3}$, for $T = 268$ K at 10.5 GHz as estimated from Eq. (5.Q.4) of Mätzler (2006) using their salinity data curve.

For ice–air mixtures of density ρ_v, the generalized mixing formula of Shivola (1989) is used with the coefficient $v = 0.85$, as recommended by Petty and Huang (2010), to determine regression equations:

$$\Re(m_r) = 0.1605\rho_v^2 + 0.7046\rho_v + 0.9988, \tag{9}$$

$$\text{if} \quad \rho_v \ge 0.3,$$

$$\Im(m_r) = -(0.0073\rho_v^3 - 0.0178\rho_v^2 + 0.0092\rho_v - 0.0014);$$

$$\text{otherwise}, \quad \Im(m_r) = 0. \tag{10}$$

2) PARTICLE DENSITY

For a particle of a given mass its volumetric density (ρ_v) enters the scattering cross-section models through both the particle size D_s and its complex refractive index m_r.

The calculation of ρ_v for different solid habits from the Mitchell parameters is underdetermined without some additional assumption regarding particle shape in order to calculate its volume. The particle is approximated by an oblate spheroid with vertically pointing minor axis (D_{thick}) and horizontal cross-sectional area equivalent to A. The axial ratio is defined as $r = D_{\mathrm{thick}}/D_{\max}$. Assumed values for r are given in Table 1.

The volume of the oblate spheroid is

$$\mathrm{Vol} = \frac{2}{3}D_{\mathrm{thick}}A. \tag{11}$$

The volumetric density is

$$\rho_v = \frac{m}{\left(\frac{2}{3}\right)rD_{\max}A}. \tag{12}$$

Substitution for m and A from (5) and (6), respectively, gives

$$\rho_v = \left(\frac{3\alpha}{2r\gamma}\right)D_{\max}^{\beta-\sigma-1}. \tag{13}$$

The scattering cross-section calculation of a particle of mass m requires the calculation of D_s from (1) and ρ_v from (5) and (13).

4. FOM and plots for Doppler spectral modes

For both real-time measurements and simulations the modal velocity and power are determined for each Doppler spectrum in the 1-min average (appendix B). The POSS used for the field measurements in this study measures about 380 Doppler spectra per minute. One of the real-time outputs from the system is a 2D frequency of occurrence matrix (FOM) of the modal power versus modal Doppler velocity. This matrix can be represented graphically where the pixel color given in the legend represents the number of occurrences in each bin. Figure 2a gives an example of a 1-min measurement during a rain event.

The v_{dop} bin resolution (x axis) is 0.223 m s^{-1}. Note that the modal velocity bins are for v_{dop}, not v_t. The sampling frequency of 2.048 kHz determines the maximum unambiguous v_{dop} of about 14 m s^{-1}. Aliasing of power from larger velocity particles is filtered by a low-pass filter in the POSS electronics. Hail with v_{dop} exceeding this maximum will not be detected.

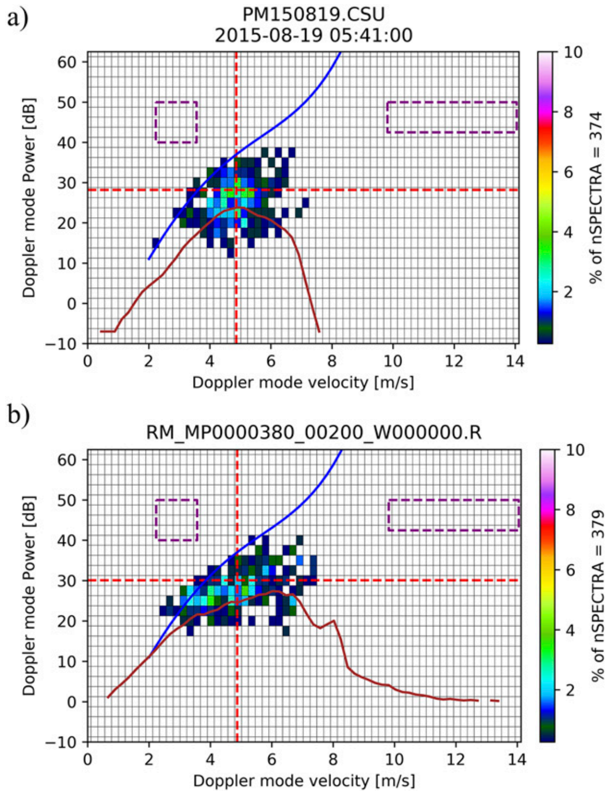

FIG. 2. (a) Plot of frequency of occurrence matrix (FOM) for spectral modes measured during 1 min of rain ending at time stamp 0541 UTC 19 Aug 2015 compared to (b) simulated rain assuming a M-P distribution at 2 mm h^{-1} for calm wind conditions. The modal centroid (mean modal velocity and power) of the distribution is at the cross hairs. The blue curve is the simulation maximum modal spectrum for liquid drops at the hot spot. The red curve is the 1-min average Doppler spectrum. The left- and right-hand boxes are the modal regions defined to be exclusively graupel and hail, respectively (section 6).

The resolution in modal power (y axis) is 2.5 dB. The POSS power units are an arbitrary scale. For the FOM, the minimum reportable power is −10 dB and the maximum is 50 dB. Occurrences of powers exceeding 50 dB are accumulated at this maximum level. This "clipping" effect is usually obvious on FOM plots and does not affect the precipitation typing algorithm described below. The clipping occurs for modal power corresponding to a liquid sphere with $D_s = 2.5$ mm located at the hot spot.

Figure 2 indicates the modal centroid (mean modal velocity and power) of the distribution at the cross hairs.

The red curve is the 1-min average Doppler spectrum. It may show spectral features that are not detected as modes of the individual spectra composing the average, e.g., in Fig. 2b at about 7.8 m s^{-1}.

The blue curve is a regression fit to a set of simulated modal centroids generated when a single raindrop traverses the hot spot. The simulation is performed for the set of $D_m(j)$ corresponding to the set of $v_{\mathrm{dop}}(j)$ in the Doppler spectrum. This curve is referred to here as the maximum modal spectrum (MMS). It can be generated for any habit and wind condition. It represents a first-order upper limit when measuring or simulating naturally occurring particle distributions randomly located in the measurement volume. It is a useful confirmation of the system's calibration when compared with measurements.

Figure 2a shows an example of the FOM of spectral modes measured during 1-min at 0541 UTC 19 August 2015. Identically sized raindrops at different locations in the measurement volume may produce different modes because of the bistatic geometry and the nonuniformity of the combined antenna pattern. At higher velocities (larger diameters), the lower number concentration have a lower probability of a sample located at the hot spot (S2007) and the modal power can be several decibels lower than the MMS. For the midrange diameters, the maximum modal power approaches the MMS curve indicating that at least one sample during the 1-min average was near the hot spot. At the lower velocities, the increase in number concentration may result in multiple raindrops contributing to the same mode. Some occurrences with modal powers greater than the MMS curve are seen in this example.

For comparison, Fig. 2b shows the simulated data also for 1 min of rain assuming an M-P distribution for a rate of 2 mm h^{-1} in calm conditions. The agreement is good showing the same pattern described above.

5. Modal centroid plots

The simulator can be used with the statistical bootstrap method (Wilks 1995) to generate 1-min sample modal distributions of centroids for 124 separate classes of precipitation specified by habit, precipitation rate, and wind condition (Table 2). These are plotted in Fig. 3a for 21 bootstrap samples per class. These distributions are central to the analysis that follows and are described in detail in this section.

a. Effect of particle size distribution on modal centroid

All of the PSD models described in section 3a are functions of precipitation rate. In general the number concentration of larger

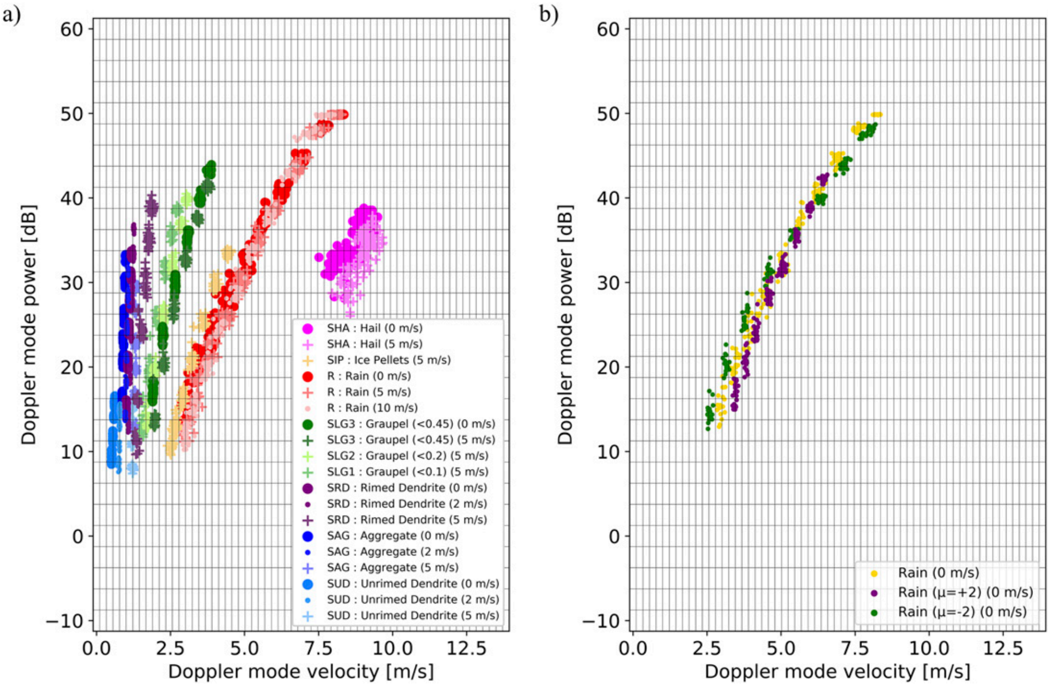

FIG. 3. (a) Bootstrap distributions of simulated modal centroids for different habits, precipitation rates and randomly oriented horizontal wind conditions. (b) As in (a), but for only rain in calm conditions comparing the M-P distribution to the modified gamma for $\mu = -2$ and $\mu = 2$.

D_m particles increases with rate. This will shift the modal centroid to greater power and velocity. For a specified habit and wind speed the modal centroid increases monotonically with rate. At very low rates the distributions for the different habits converge.

The sensitivity of the modal distribution to the shape of the PSD is demonstrated in Fig. 3b by comparing the M-P distribution to the modified gamma distribution in rain for values of $\mu = -2$ and 2 for calm conditions. The slope of the modal distributions as a function of rate differs slightly.

b. Effect of wind on modal centroid

The effect of wind speed on the modal centroid is also evaluated from Fig. 3a. Both the direction and magnitude of the wind affect the Doppler spectrum generated by a single particle. The effect is least if the wind is oriented along the axis of the transmitter and receiver. In the absence of information regarding actual wind direction in the POSS measurement volume, it is assumed to be randomly oriented in the simulations. For a given habit and precipitation rate, wind shifts the modal velocity from the corresponding calm condition by amounts much less than the wind speed itself. The magnitude of the shift depends on the terminal velocity. At lower velocities associated with unrimed dendrites and aggregates, the wind increases the modal velocity. For higher terminal velocities, e.g., in graupel and rain, the change is smaller. The consequence of wind shifts is to cause the modal distributions of some types to overlap, for example, rimed dendrites in calm condition and unrimed dendrites at 5 m s^{-1}.

Increased wind speed increases the variance and the maximum of the 1-min modal velocity distribution. Increased wind speed will also decrease the maximum modal power in the 1-min modal distribution because the length of time each particle is sampled in the hot spot volume is reduced compared to calm conditions.

When analyzing data from field experiments using operational reports of wind speed it should be remembered that these are typically measured at 10 m elevation. Operationally reported speed will be greater (approximately a factor of 2) than those experienced at the POSS installation height (nominally 3 m). Future field experiments would benefit from measurements of wind speed and direction at the POSS sensor height.

c. Effect of particle density and phase on modal centroid

For the same particle mass both v_t and the scattering cross section (for non-Rayleigh particles) will depend on volumetric density (ρ_v). The distribution of modal centroids will vary for a specific habit if the density is changed. For example, the centroid distribution is given for three lump graupel density ranges (0.05–0.1, 0.1–0.2, and 0.2–0.45 g cm^{-3}) using the corresponding Mitchell parameters from Locatelli and Hobbs (1974, hereafter LH1974). In general, for the same wind and PSD, the distributions shift to larger velocity and power as the density increases.

The combined effect of two factors results in some overlap in the centroid distributions of rain and ice pellets for the same PSD. The refractive index factor for ice reduces its scattering power by about 6.5 dB compared to a liquid drop of equivalent mass in the Rayleigh scattering size range. However, the v_t of ice pellets is also reduced from that of raindrops of the same mass because of differences in the drag coefficient due to the roughness of the surface. These two effects shift the centroid distribution to lower powers and velocities so that there is a partial overlap of the two in the modal centroid space.

TABLE 2. Multiple discriminant analysis (MDA) class and group names. Note that "rate" column gives the range of precipitation rates in steps of a factor of 2.

Class	Rate (mm h^{-1})	Wind (m s^{-1})	Class group name
1–15	0.125–2.000	0.0, 2.0, 5.0	Unrimed dendrite
16–33	0.125–4.000	0.0, 2.0, 5.0	Aggregate
34–51	0.125–4.000	0.0, 2.0, 5.0	Rimed dendrite
52–57	0.125–4.000	5.0	Graupel < 0.1 g cm^{-3}
58–63	0.125–4.000	5.0	Graupel < 0.2 g cm^{-3}
64–75	0.125–4.000	0.0, 5.0	Graupel < 0.45 g cm^{-3}
76–105	0.125–64.000	0.0, 5.0, 10.0	Rain
106–112	0.125–8.000	5.0	Ice pellets
113–124	1.000–32.000	0.0, 5.0	Hail

Also the terminal velocity of ice pellets is sensitive to their shape and orientation. Nagumo and Fujiyoshi (2015, hereafter NF2015) found variations as large as a factor of 5 for the same diameter.

6. Multiple discriminant analysis

MDA (Wilks 1995) is used to assign the measured data to a specific class as defined by a "training set" of simulated bootstrap data. There are currently 124 classes (Table 2). The data vector used in this analysis consists of 7 elements ("features") derived from the 1-min modal distributions. The features are the mean modal velocity and its variance, the mean modal power and its variance, the maximum modal velocity, the maximum modal power, and the zeroth moment of the 1-min average Doppler spectrum in units of dB. In the future if wind information is available, it could also be included in the data vector.

This seven-element data vector is transformed to the corresponding principal coordinate basis using principal component analysis (PCA) (Wilks 1995). The discriminant analysis is then carried out using the five principal components that account for the largest fraction of the total variance. Both the PCA and MDA analyses are implemented using the International Mathematical and Statistical Library (IMSL; IMSL 2018) software.

The success of this method depends on the separation of the modal distributions associated with each habit, PSD, and wind condition. As mentioned earlier the wind can cause classes with slower velocities to overlap. In the case studies (section 7) the wind speed is estimated from the observations at nearby Greeley airport. For rimed and unrimed dendrites, and aggregates only the classes with wind speed closest to the Greeley-based estimate were included in the MDA training set. This restriction was not applied to the other types as they were less affected by wind.

Also note that rain and ice pellets are closely spaced which may cause an unrealistic number of ice pellet reports. The MDA software can assign a priori probabilities to each class. Ice pellets are given a low probability in order to minimize false identification.

If the precipitation is mixed during the 1-min measurement the data vector derived from the modal distribution will be weighted by the proportions and scattering cross sections of the different precipitation types. This could result in missing the occurrence of the less dominant type entirely. Specific precipitation types can be identified by the occurrence of modes in restricted regions of the modal space. These regions are determined by a priori examination of the simulation results for a range of precipitation rates and wind speeds. The objective is to define a modal region that maximizes the probability of detection of a single type in mixed precipitation, e.g., hail or graupel, while minimizing false identifications of these types. For example, rain at high precipitation rates and wind speeds may have occurrences of modal velocity and power where hail would occur in calm conditions. This restricts the range of the modal space unique to hail.

The dominant precipitation type is determined using MDA analysis for a data vector derived from the full modal space range. The precipitation type is determined as mixed if there are any occurrences in a restricted modal space range (defined by the boxes in Fig. 2) different from the dominant type.

7. Case studies

Case studies are presented in different precipitation types from the MASCRAD site at Easton. MASC images are used to validate POSS MDA results, and the maximum dimension in the plane of the image is given in the Figure. The MASC images

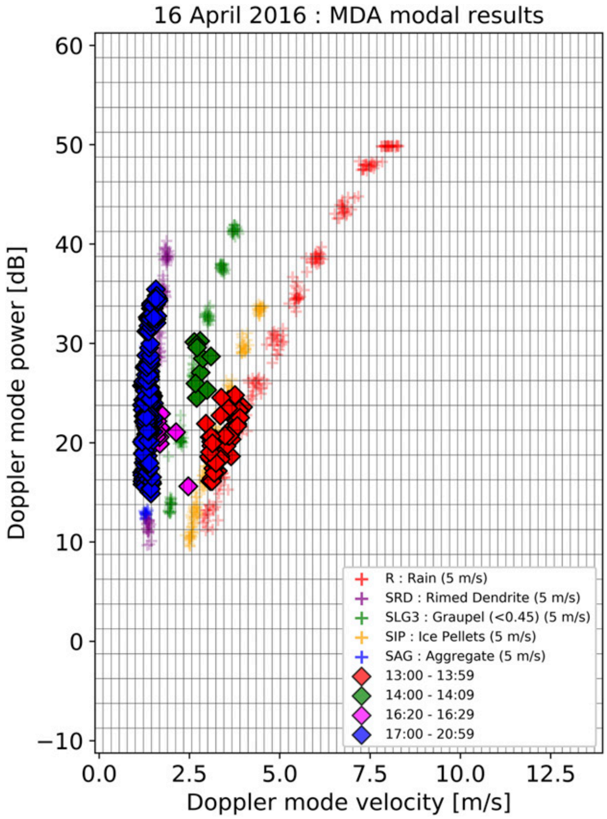

FIG. 4. The 16 Apr 2016 comparison of 1-min measured modal centroids (diamonds) to simulated class centroids (crosses) from a subset of Fig. 3a that best corresponds to the 5 m s^{-1} wind speed measured at Greeley Airport. This shows the transition of centroids from rain (1300–1359 UTC, red), to graupel (1400–1409 UTC, green), to rimed dendrites (1620–1629 UTC, pink), to aggregates (1700–2059 UTC, blue).

are time stamped with 1-s resolution, while the POSS data resolution is 1 min and time stamped at the end of its 60-s measurement window. Furthermore, although the POSS clock is synchronized to UTC its acquisition period is free running and does not necessarily begin at the start of each new minute.

In general it is difficult to simulate the wind effect in a quantitative way as the nearest measurements are operational from the Greeley Airport 13 km distant. For MASCRAD the POSS was mounted above the top of a double fence wind shield. The wind speed in the POSS measurement volume is unknown and can only be estimated from the Greeley data.

Comparisons of plots of the 1-min measured modal centroid to the simulated distributions given in Fig. 3a are instructive in analyzing transitions in precipitation type (e.g., Fig. 4 for case 1, 16–17 April 2016).

MDA classification is plotted as a time series (e.g., Fig. 5 for case 1, 16–17 April 2016). The 124 classes are grouped into 9 types (Table 2) for the purposes of simplifying the time series plots. All times are UTC. There is only one value for each minute from each MDA filter but there may be simultaneous occurrences for the two different time series, e.g., "MDA" and "graupel."

The classes have been ordered on the *y* axis according to increasing range of modal centroid velocities. For clarity, all classes of the same type, regardless of wind and precipitation rate, have been plotted as a single class. The zeroth moment of the POSS Doppler spectrum (an indication of precipitation rate) is given in a separate panel.

a. *Case 1: 16–17 April 2016*

Figure 4 shows POSS centroid measurements for 4 periods during the transition from rain (1300–1359 UTC, red), to graupel (1400–1409 UTC, green), rimed dendrites (1620–1629 UTC, pink) to aggregates (1700–2059 UTC, blue) superimposed on a subset of simulated classes for a wind speed of 5 m s^{-1} (estimated from Greeley observations) given in Fig. 3a. The transition from faster to slower modal velocities is evident.

Figure 5 shows a time series of the measured POSS MDA for the entire event. At selected times, corresponding MASC images are shown in the margins. The wind speed ranges from 5 to 9 m s^{-1} with gusts >10 m s^{-1}. MDA identification is primarily rain mixed with other solid types prior to 0119 UTC at which time unrimed dendrites first occur.

The graupel region of modal space indicates some occurrences which MDA identified as rain (e.g., 0349 UTC 16 April 2016). It is possible that these were periods of mixed precipitation. At other times both analyses indicated graupel.

From 1300 to 1900 UTC 16 April 2016 MDA shows a transition from rain through graupel, rimed dendrites, aggregates to unrimed dendrites. Visual examinations of a number of MASC images were made during the graupel period from 1400 to 1410 UTC 16 April 2016 (e.g., Fig. 5a). The particle size and clarity varied widely, but many instances were observed when the particle roughness and opacity were consistent with the optical characteristics of graupel. MDA classified a mixture of rimed dendrites mixed with the graupel from 1604 to 1645 UTC 16 April 2016 (e.g., Figs. 5b,c). Aggregates occurred more frequently after 1700 UTC 16 April 2016 (Figs. 5d,e). From 1851 to 2143 UTC 16 April 2016 the precipitation type reverses the sequence from aggregates to rimed dendrites to graupel and finally rain. Around 0000 UTC 17 April 2016 the earlier pattern

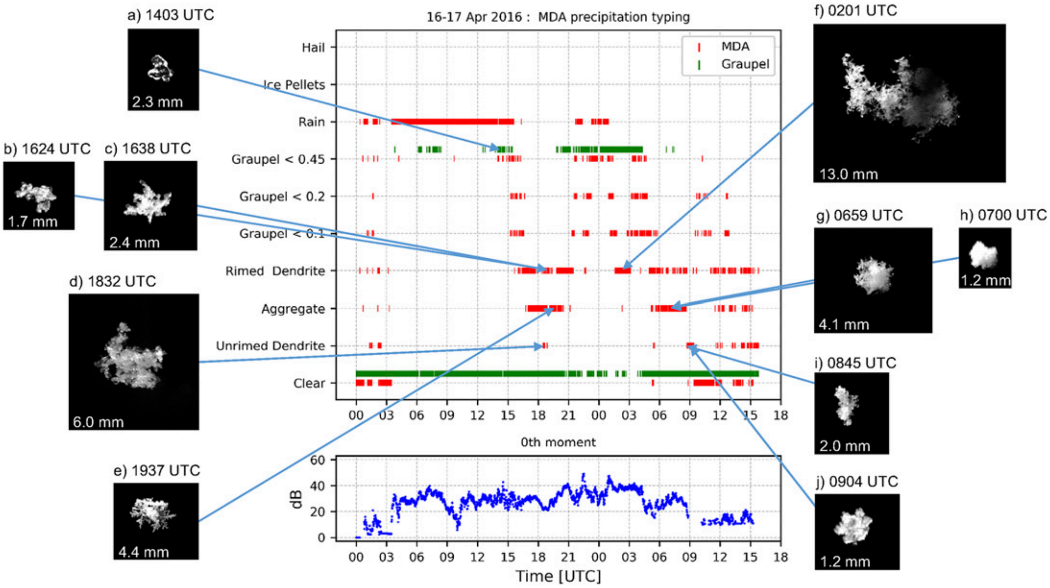

FIG. 5. Time series of MDA precipitation type for the transition event case 1: 16–17 Apr 2016. (top) The 1-min MDA precipitation type (labels on left-hand axis) are represented as red symbols (for MDA analysis labeled "MDA") and green symbols (graupel filter analysis labeled "graupel"). (bottom) The POSS zeroth-moment (dB arbitrary units). Corresponding sublabeled MASC images are shown in the margins, along with their maximum dimension (mm) in the plane of the image, and call out arrows to their MDA results location in time and habit.

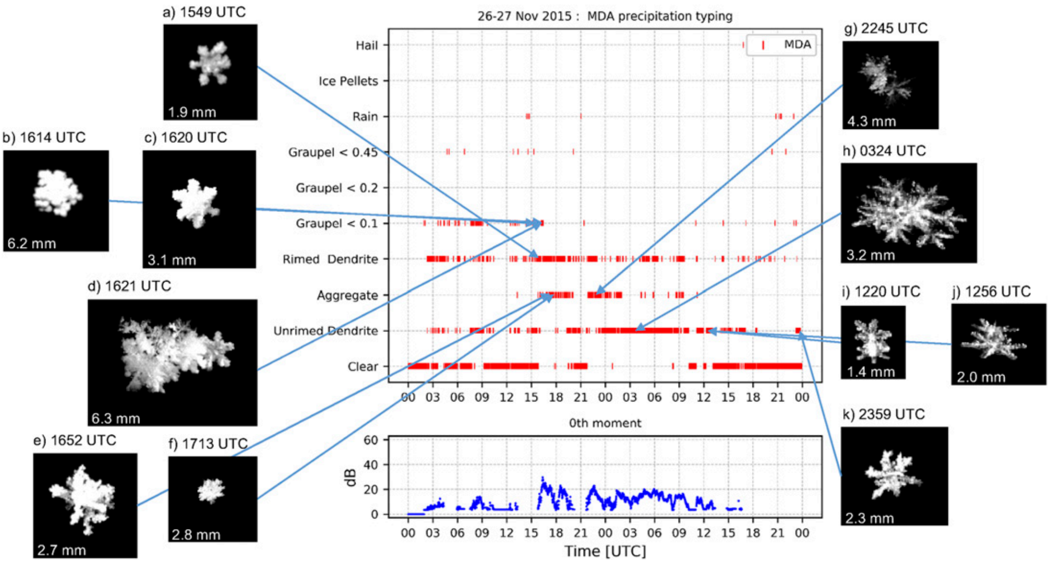

FIG. 6. As in Fig. 5, but for case 2: 26–27 Nov 2015.

from rain through graupel, rimed dendrites, aggregates to unrimed dendrites (Figs. 5f–j) is repeated. After 0925 UTC another transition (graupel–rimed dendrites–aggregates–unrimed dendrites) begins.

b. Case 2: 26–27 November 2015

Hydrometeor images collected by the MASC at the Easton site indicated that a fairly high degree of riming was present during the period of 1600–2000 UTC 26 November 2015; less riming was identified later in the period of 0200–0430 UTC 27 November 2015 (Kennedy et al. 2018). Figure 6 contains example MASC images from these two time segments. The wind speed at Greeley was 3 to 5 m s^{-1}.

From 1548 to 1730 UTC 26 November 2015 POSS most frequently identified rimed dendrites. From 1730 to 2000 UTC aggregates were mixed with the rimed dendrites. From 2200 to 2300 UTC the proportion of rimed dendrites decreased, and after 2300 UTC, POSS identified a mixture of unrimed dendrites and aggregates with the latter becoming infrequent by 0200 UTC 27 November 2015.

c. Case 3: 7 March 2016

This event starts with rain at 1737 UTC mixed with short intervals of both hail and graupel. The hail region of modal space first reports occurrences at 1755 UTC (blue symbols in Fig. 7) and this is confirmed by the MASC image in Fig. 7a.

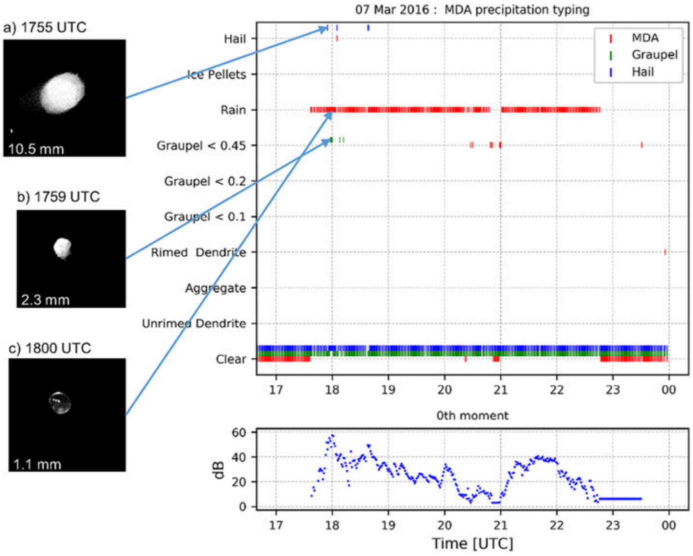

FIG. 7. As in Fig. 5, but for case 3: the 7 Mar 2016 graupel event.

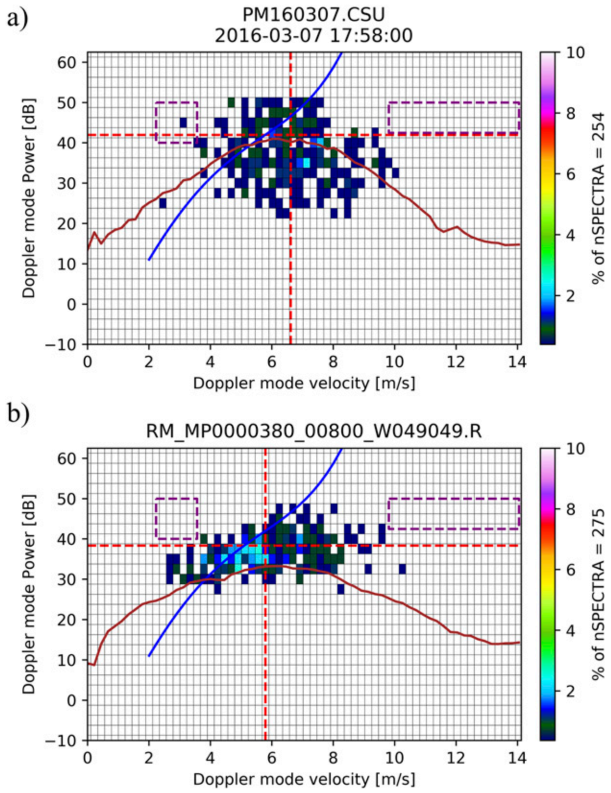

FIG. 8. (a) FOM plot for spectral modes measured during 1 min of rain ending at time stamp 1758 UTC 7 Mar 2016 compared to (b) simulated rain assuming a M-P distribution at 8 mm h^{-1} for 7 m s^{-1} wind conditions.

The mean wind is 12.9 m s^{-1} gusting to 17.5 m s^{-1}. The graupel region first reports occurrences at 1758 UTC and some additional minutes up to 1812 UTC (green symbols in Fig. 7). At 1758 UTC Fig. 8a shows that single Doppler spectral modes occur in the modal graupel region but the majority are in the rain region. For comparison Fig. 8b plots the FOM diagram for a simulated M-P distribution in rain at a rate of 8 mm h^{-1}, without the presence of graupel, for a wind speed at POSS height of 7 m s^{-1}. The MASC images support both graupel (Fig. 7b) and rain (Fig. 7c) at this time.

After this period, rain is reported in agreement with the MASC images.

d. Case 4: 7 May 2016

Hail was observed during this event. MDA results in Fig. 9 reported 15-min of hail from 1928 to 1947 UTC (red symbols). The hail modal range identifies 28 min as hail between 1941 and 2038 UTC (blue symbols).

Figure 9a shows a MASC image of a hailstone of size 4.4 mm at 2009 UTC. The FOM of measured modes for 1-min ending at 2010 UTC (Fig. 10a) is compared to a single bootstrap simulation sample in rain for a rate of 16 mm h^{-1} and mean wind speed of 5 m s^{-1} (Fig. 10b). The hail component is evident from the number of occurrences in the upper right box. The maximum measured Doppler velocity mode is about 12.7 m s^{-1} equivalent to a terminal velocity of about 14.0 m s^{-1} corresponding to a hailstone of $D_{\max}$ = 10.9 mm using the HM2010 formulation. The stone in Fig. 9a appears to be melting which could result in a "brightband" effect. Several modal powers are at or above the clipping level of 50 dB.

Figure 11 shows a series of 1-min FOM plots for the 2043 to 2046 UTC period in which a mix of hail and rain are apparent. This is supported by the MASC image in Fig. 9b showing both a raindrop in the lower right and an ice sphere in the upper left. The corresponding POSS FOM plot at 2044 UTC in Fig. 11b shows a maximum v_{dop} mode at about 12.3 m s^{-1}. However, the mode did not fall within the hail modal region and was not identified by POSS. Figure 9c shows another MASC hailstone within 2 min, and is likely evidenced by the POSS FOM points >10 m s^{-1} in Fig. 11c.

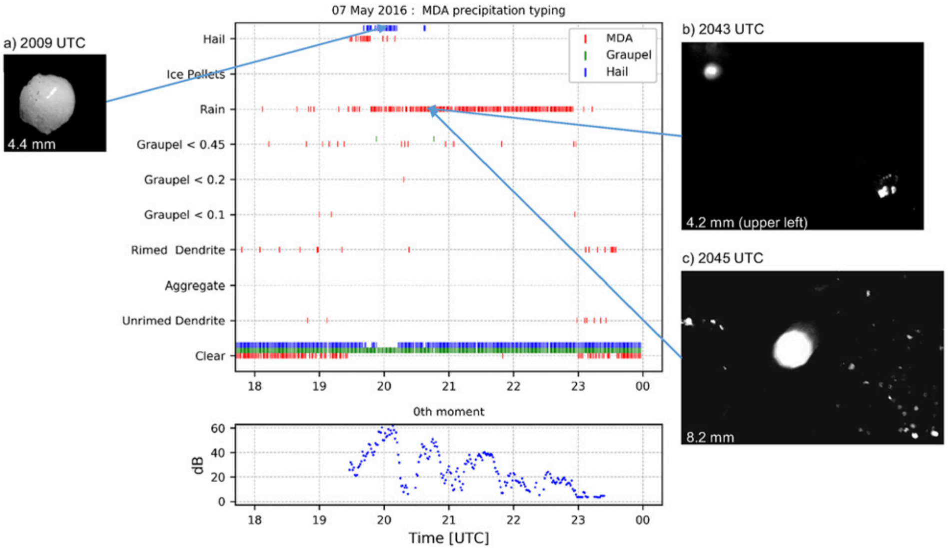

FIG. 9. As in Fig. 5, but for case 4: the 7 May 2016 hail event.

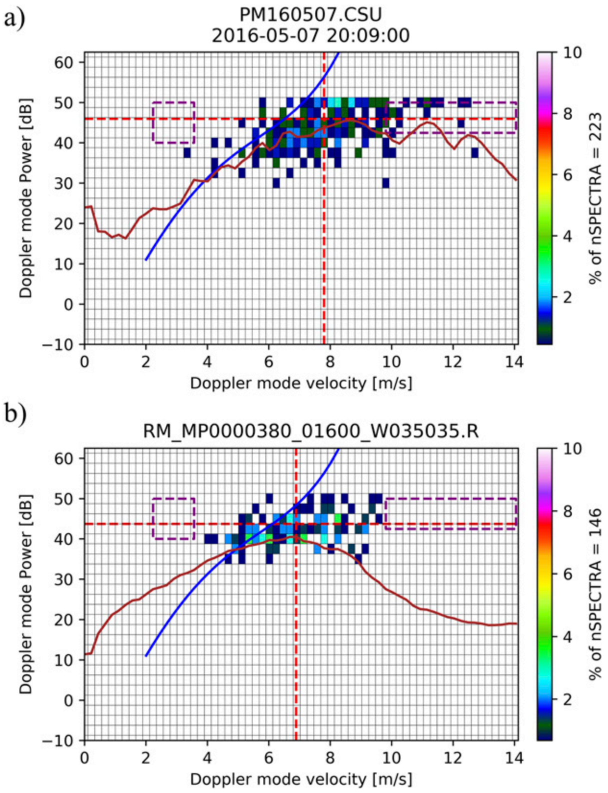

FIG. 10. (a) FOM plot comparing spectral modes measured during 1 min of rain and hail ending at 2009 UTC 7 May 2016 and (b) bootstrap simulation of rain only with an M-P rate of 16 mm h^{-1} in 5 m s^{-1} wind. The box in the upper-right corner is the modal space used to identify hail.

8. CSU–CHILL dual-polarization radar data during the four POSS hydrometeor classification cases

The POSS installed at the Easton site is located at a range of 13 km from the dual-wavelength, dual-polarization CSU–CHILL radar (Junyent et al. 2015). An overview of the Easton–CSU–CHILL observing network is available in Bringi et al. (2017, their Fig. 1). The close separation between Easton and CSU–CHILL allows the collection of dual-polarization data at wavelengths of 11 and 3 cm (S and X bands, respectively) at heights between approximately 150–225 m above the POSS sample volume. In this section, samples of CSU–CHILL data collected during selected periods in the four POSS case studies are presented.

CSU–CHILL X-band radar data from the 16 April and 7 March 2016 events (cases 1 and 3) are shown by the color-coded dots in Fig. 12. The data are from the individual range gate measurements that were collected during 0.9° elevation PPI sweeps within an azimuth interval of ±0.5° and a range interval of ±0.15 km with respect to the POSS. Data from two time periods during 16 April 2016 (case 1) are shown by the purple and green dots. The POSS hydrometeor identification algorithm identified several particle type transitions during this event (see Fig. 5). The 16 April 2016 radar data plotted in Fig. 12 were taken from two time periods when the POSS modal-based algorithm identified two distinctly different precipitation types. In the 1300–1400 UTC hour (purple dots), a rain was diagnosed. Later in the same event, between 1700 and 2000 UTC (green dots), the processing of the POSS data determined that various forms of snow were the predominant hydrometeor form. (Also, local weather observations made by the radiosonde launch crew at Easton reported steady, wet, sticking snow at 1824 UTC.) These POSS classifications are consistent with the CSU–CHILL X-band data. During the 1300–1400 UTC hour, reflectivities were in the 20–28 dBZ range with Z_{dr} values clustered around 0 dB. This combination is typical of the quasi-spherical shapes associated with small diameter raindrops and irregular graupel particles. During the subsequent snow period (1700–2000 UTC), CSU–CHILL reflectivity levels averaged ~7 dB lower. A wider range of Z_{dr} values were observed, with positive Z_{dr} values of up to ~+1 dB occurring in association with the lowest reflectivities. This shift toward more positive Z_{dr} values (green dots in Fig. 12) relative to the

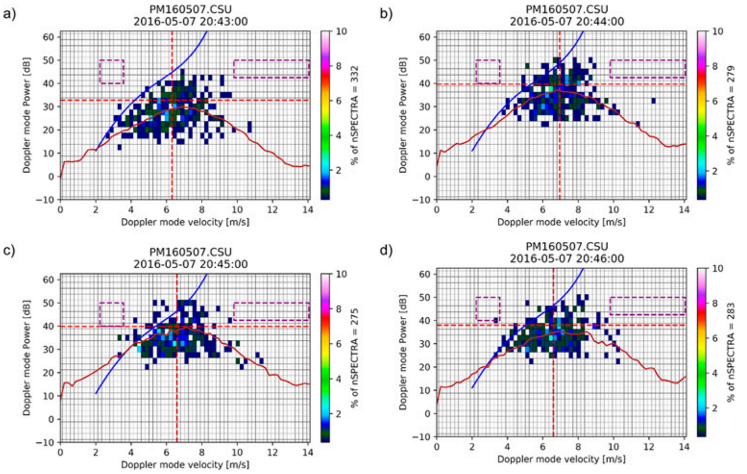

FIG. 11. As in Fig. 10a, but for 1-min intervals during the period 2043 to 2046 UTC corresponding to MASC images in Figs. 9b and 9c showing mixed hail and rain.

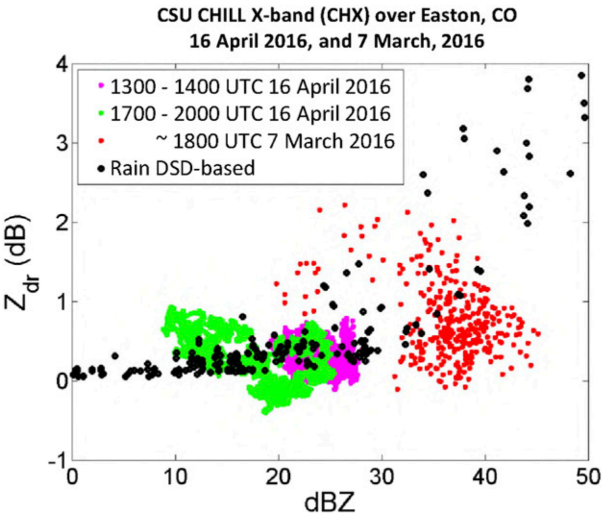

FIG. 12. CSU–CHILL X-band Z_{dr} vs Z gate data plots for MASRAD POSS cases 1 (16 Apr 2016) and 3 (7 Mar 2016).

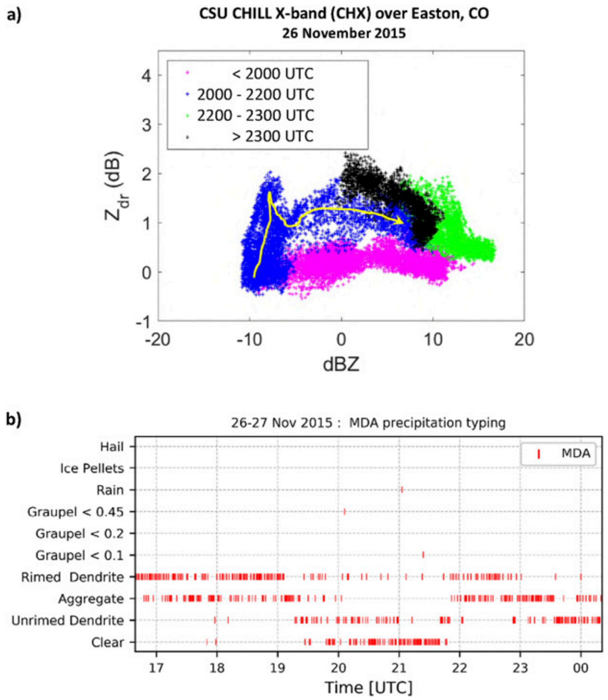

FIG. 13. (a) CSU–CHILL X-band gate data for MASRAD POSS case 2 (26–27 Nov 2015). (b) POSS MDA precipitation typing for 1700 to 2400 UTC 26 Nov 2015.

earlier 1300–1400 UTC time period is consistent with the disappearance of the more spherical graupel particle types and the appearance of several types of snow, including some unrimed dendrites around 1830 UTC in the POSS classifications (Fig. 5).

The red dots in Fig. 12 show the X-band CSU–CHILL radar data collected during the period of 1700–1800 UTC 7 March 2016; the MASC camera images and POSS identifications included mixed rain, graupel and hail near 1800 UTC (case 3, Fig. 7). The center of the primary cluster of red dots in Fig. 12 is located around 40 dBZ and ~0–0.2 dB in the CSU–CHILL X-band parameter space. For reference, the black dots in Fig. 12 show the Z, Z_{dr} values were obtained from backscattering calculations made by assuming that the particle distributions assembled from combined 2DVD and PMS size spectra were composed entirely of water. Additionally, the diameter aspect ratio formulation from Thurai et al. (2007) was applied. The objective of these efforts was to provide the Z_{dr} versus Z behavior expected if the hydrometeor spectra observed during the 1700–1800 UTC hour were composed entirely of raindrops. The distinct tendency for the observed Z–Z_{dr} values (red dots) to fall below the Z_{dr} levels expected for pure rain (black dots), especially at higher reflectivity values, is consistent with the presence of mixed graupel and hail particles whose ice structure resists the aerodynamic deformation experienced by falling raindrops.

CSU–CHILL X-band radar Z_{dr} versus Z time histories for portions of case 2 (26–27 November 2015; Fig. 6) are shown in Fig. 13. The colors used to plot the radar data points differentiate a sequence of four time periods of interest: magenta between 1725 and 2000 UTC, blue between 2000 and 2200 UTC, green between 2200 and 2300 UTC, and black between 2300 and 2354 UTC. During the first time period (before 2000 UTC), the Z_{dr} values remained near 0 dB. This is characteristic of reflectivity-weighted mean hydrometeor shapes that are quasi-spherical or nonspherical particles with no preferred orientation. In the intermediate period (2000–2200 UTC), the CHILL X-band reflectivities became very low while the maximum Z_{dr} values increased to ~+2 dB levels. These dual-polarization signal characteristics are consistent with a low concentration of unaggregated, fairly pristine snow crystals. The yellow arrow in Fig. 13 traces the general time evolution of the plotted radar characteristics during the 2000–2200 UTC transition period (blue dots). From the initial near 0 dB Z_{dr} values observed at the end of the earlier, more highly rimed regime, Z_{dr} rose to its peak levels during the minimal reflectivity, pristine crystal period. During the final two time periods (after 2200 UTC), the distribution of green and black data points assumed the negatively sloped configuration in Z_{dr} versus Z space that is typical of light snowfall containing a combination of larger aggregates coexisting with more oblate single crystals.

These four inferred hydrometeor regimes generally agree with the POSS classifications shown in Fig. 13b. From 1548 to 1730 UTC POSS most frequently identified rimed dendrites. From 1730 to 2000 UTC aggregates were mixed with the rimed dendrites. The aerodynamic and mass redistribution effects of this rime accumulation probably induced larger fluctuations in the snow particle orientation (Kennedy et al. 2018), tending to reduce Z_{dr}. During the 2000–2200 UTC very low reflectivity period, POSS identifications are unrimed and rimed dendrites. From 2200 to 2300 UTC there was a mixture of rimed dendrites and aggregates, and 2300–0000 UTC, POSS identified a mixture of unrimed dendrites and aggregates with the latter becoming infrequent by 0200 UTC the following day. This hydrometeor population is consistent with the negatively sloped Z_{dr} versus Z CSU–CHILL X-band data regime. Note also from Fig. 13 that

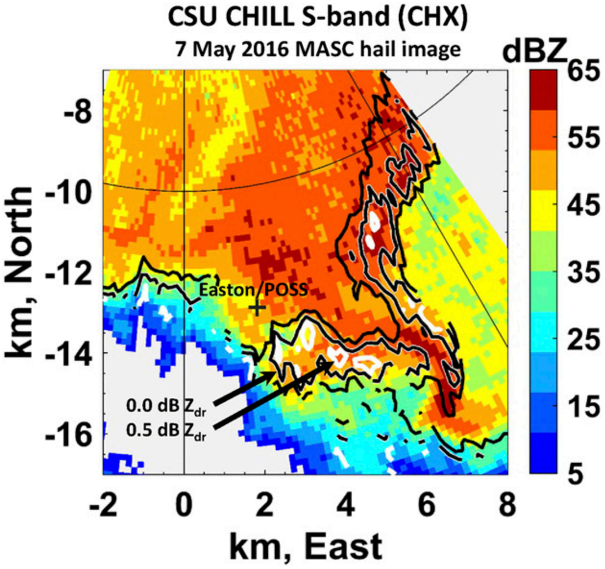

FIG. 14. CSU–CHILL S-band (11 cm wavelength) reflectivity levels (color fill, dBZ) in a PPI scan at 0.5° elevation angle at 2009 UTC 7 May 2016 (see case 4, Fig. 9a for MASC image). Contour overlay identifies two low Z_{dr} levels: the white contours are for Z_{dr} of 0 to 0.5 dB and the black contours are for Z_{dr} of 0.5 to 1.2 dB.

for 2200–2300 UTC we see higher dBZ and lower Z_{dr}, which is consistent with the higher POSS spectral zeroth moments associated with rimed dendrites. Rimed particles tend to be more spherical-like than unrimed dendrites which would be expected to exhibit higher Z_{dr} values as we see from the radar observations after 2300 UTC. Hence the transition from rimed dendrites and aggregates to unrimed dendrites and aggregates as seen from the POSS-based classification at around 2300 UTC is supported by the CHILL data in Fig. 13.

Figure 14 shows CSU–CHILL S-band (11 cm wavelength) data in a 1.9° elevation angle PPI scan taken during POSS case 4 when hail was identified on 7 May 2016 (Fig. 9). The white contours overplotted in Fig. 14 identifies area where Z_{dr} is less than 0.5 dB; the black contours depict Z_{dr} levels between 0.5 and 1.2 dB. The combination of high ($\gtrsim$45–50 dBZ) reflectivity and low Z_{dr} in convective precipitation shafts at near-surface heights is a well-established indication of hail (Herzegh and Jameson 1992). As the thunderstorm shown in Fig. 14 moved northward, a portion of the area with high Z and near 0 dB Z_{dr} crossed the POSS site at the time of the hail identifications in Fig. 9 around 2000 UTC. The hail indications in this PPI scan are consistent with the hailstone image that was captured by MASC at 2209 UTC (Fig. 9a).

Additional confirmation of hail was obtained approximately 17 min after the PPI scan data when small hailstones were collected at the CSU–CHILL radar site (Fig. 15). The photographed stones were collected from the ground as the precipitation intensity decreased, hence melting probably reduced the diameters by the time of the photograph. Since the American Meteorological Society Glossary of Meteorology (American Meteorological Society 2020) defines hail as having a minimum diameter of 5 mm, the photographed ice particles in Fig. 15 agree with the hail hydrometeor identification made by POSS for 28 min during the period from 1941 and 2038 UTC (Fig. 9).

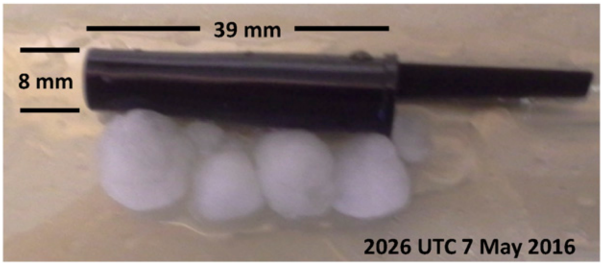

FIG. 15. Digital photograph of several small hailstones collected at the CSU–CHILL radar site near 2026 UTC 7 May 2016 (see case 4, Fig. 9) after the storm had passed the POSS at Easton. Ballpoint pen cap included as a size reference.

9. Conclusions

This article presents an analysis technique to better distinguish precipitation types, particularly for solid precipitation, by using the POSS Doppler spectral modal data. Historically the POSS has used 1-min average Doppler velocity spectra to estimate if the precipitation type was either liquid or solid. However, the POSS also records the modal power and velocity of the 380 individual Doppler spectra used in the 1-min average. These data are collected routinely as part of all field experiments but have not previously been analyzed. In this work, the power and velocity at the mode of each Doppler spectrum measured during the minute is used to find the centroid of the two-dimensional modal distribution.

A new simulation model was developed to generate the time domain Doppler signal measured by POSS for a variety of precipitation types and particle size distributions in different wind conditions. The simulation model, with bootstrap sampling, generates training sets of variables, including the modal centroid of the distribution, for a variety of precipitation types and rates and wind classes. The training set is input to multiple discriminant analysis (MDA) software to classify POSS measurements as to different solid and liquid precipitation types. The effect of wind on the training set is discussed. An approach for identifying mixed precipitation events is given.

Four case studies compare POSS typing estimates to images made by MASC during the MASCRAD experiment (2015–16) in Easton, Colorado, and to CSU–CHILL radar observations. This technique successfully identified transitions of precipitation type as well as hail events as confirmed both from MASC images and radar observations. At this time the identification of hail, rain, graupel, rimed and unrimed dendrites, and aggregates is possible. The wind has the greatest effect on the distinction between the lower terminal velocities types. If wind information is available, then the classification of these types is improved.

The long history of POSS has evolved from a present weather sensor for automated stations to a component of field research experiments. Currently there are POSS installations at a number of international sites: Canada (Toronto, Eureka, Iqaluit), United

States (Colorado, Alabama), Greenland (Summit), and South Korea (Daegu).

Some features of POSS are not found in other surface-based sensors: a larger sample volume that is at the surface, estimation of the accumulation of very light solid precipitation over long time periods without the losses experienced by conventional gauges, and low field maintenance in harsh climates.

ECCC intends to support future field campaigns with the loan and operation of POSS. Data analysis will include the new technique presented here for the classification of precipitation type. The improved POSS-based hydrometeor classification can also act as "ground validation" for operational and research-based dual-polarization weather radar based classifications. The same applies to satellite-based radars such as the GPM-based dual-frequency precipitation radar (DPR). Further, in regions where radar coverage is limited, due to clutter contamination, beam blockage, etc., for ground-based systems, and the "blind-zone" problems associated with DPR, the new POSS-based hydrometer classification may be able to provide more reliable information. This could form possible future work.

Acknowledgments. M. Thurai received partial funding to conduct this research from National Science Foundation under Grant AGS-1901585 (PI: Prof. V. N. Bringi). We would also like to thank Prof. B. M. Notaroš for making available the image files from the Multi-Angle Snowflake Camera.

Data availability statement. POSS MDA and simulation programming and processing were by Sheppard; any further inquiries are by request.
POSS postprocessed results were provided to Rodriguez for figure production and included in the online supplement to this manuscript as "JTECH_Sheppard_data_package.tar.gz" with Attribution-Noncommercial 4.0 International licensing.
CHILL data processing and visualization as well as MASC image files used in this paper are available upon request to CSU authors.

APPENDIX A

Calculation of v_t, D_s, and ρ_v

Following the approach of HW2010, the steps for calculating v_t, D_s, and ρ_v for solids for a given D_m are as follows:

First, we calculate

$$m=\frac{\pi}{6}\rho_l\left(\frac{D_m}{10}\right)^3, \tag{A1}$$

from (1), where D_m (mm) is the diameter of a liquid sphere of the same mass, m (g), as the particle, and ρ_l is the density of liquid water (assumed 1 g cm^{-3}).

Next, the maximum dimension in the plane normal to the flow (mm) is calculated as

$$D_{\max}=\left(\frac{m}{\alpha}\right)^{1/\beta}, \tag{A2}$$

from (5), where α and β are the Mitchell parameters given in Table 1.

From (6), the area normal to the flow (cm^2) is

$$A=\delta D_{\max}^{\sigma}, \tag{A3}$$

where δ and σ are the Mitchell parameters given in Table 1.

The dimensionless area ratio is determined as

$$A_r=\frac{A}{\left(\frac{\pi}{4}\right)D_{\max}^2}. \tag{A4}$$

From (13), the volumetric density (g cm^{-3}) assuming an oblate spheroid is

$$\rho_v=\left(\frac{3\alpha}{2r\gamma}\right)D_{\max}^{\beta-\sigma-1}, \tag{A5}$$

where r is the dimensionless ratio of the minor axis to $D_{\max}$ given in Table 1.

Then, the diameter (mm) of a sphere of the same volume as the particle is calculated:

$$D_s=D_m\left(\frac{\rho_l}{\rho_v}\right)^{1/3}. \tag{A6}$$

From (8) of HW2010, the modified Best number is

$$X^*=\frac{\rho_{\text{air}}}{\eta^2}\frac{8mg}{\pi A_r^{1-k}}, \tag{A7}$$

where $\rho_{\text{air}} = 1.061\,33 \times 10^{-3}$ g cm^{-3} is the density of air at Easton, per International Standard Atmosphere (ISO 1975), g = 980 cm s^{-2} is the acceleration due to gravity, η = 1.816 × 10^{-4} g cm^{-1} s^{-1} is the dynamic viscosity of air, and k is area ratio exponent in (7) of HW2010 assumed to be 0.5 here.

From section 4 of HW2010, the dimensionless Reynolds number is

$$\text{Re}=\frac{\delta_0^2}{4}\left[\left(1+\frac{4\sqrt{X}}{\delta_0^2\sqrt{C_0}}\right)^{1/2}-1\right]^2, \tag{A8}$$

where δ_0 is the dimensionless surface roughness parameter given in Table 1 and C_0 is the dimensionless pressure drag coefficient given in Table 1.

Also from section 4 of HW2010, the terminal velocity (m s^{-1}) can be calculated as

$$v_t=\left(\frac{\eta\text{Re}}{\rho_{\text{air}}D_{\max}}\right)\Big/100. \tag{A9}$$

APPENDIX B

Steps in the Simulation of the POSS Doppler Velocity Spectra Measurement

Figure B1 gives the steps performed to simulate the Doppler velocity voltage measured by POSS for a given habit, PSD, and wind conditions. Figure B2 gives the steps to simulate the

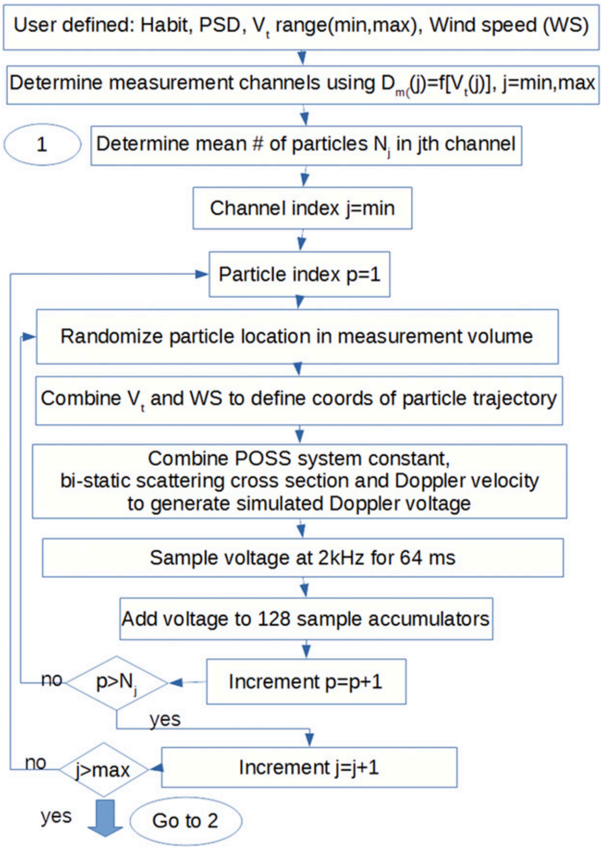

FIG. B1. Steps in simulation of POSS Doppler velocity voltage.

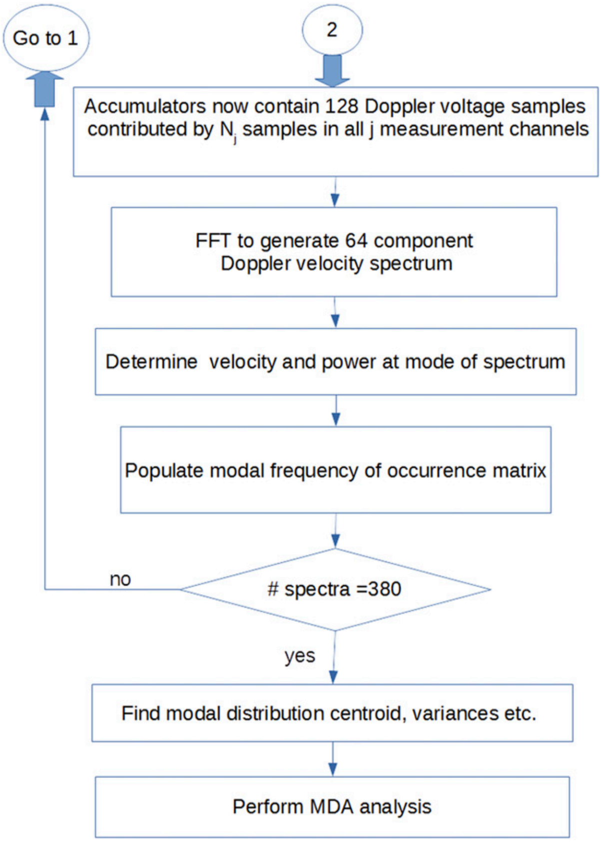

FIG. B2. Steps in simulation of POSS Doppler velocity spectrum and MDA analysis.

centroid of the modal distribution of 380 spectra measured during the 1 min.

The center of the jth POSS measurement channel is defined by the Doppler velocity spectral component $v_{\text{dop}}(j) = 0.223j$, where 0.223 m s^{-1} is the spectral resolution. The $D_m(j)$ corresponding to this center is found for solid precipitation by inversion of the terminal velocity equation (section 3b) and conversion of $v_t(j)$ to $v_{\text{dop}}(j)$ using (4). The $D_m(j) = f[v_t(j)]$ for several habits are given in Fig. 1. The channel diameter width is defined by the $D_m(j)$ boundaries corresponding to $v_{\text{dop}}(j) \pm 0.1115$ m s^{-1}.

The number of particles sampled in each of the jth measurement channels is assumed to have a Poisson distribution with mean determined from the PSD for a fixed measurement volume size. The particles are distributed randomly throughout the measurement volume at the start of the measurement sampling window and traverse the volume with velocity vectors which are the resultant of their terminal velocity and a specified wind. The resultant composite Doppler voltage from all particles in the PSD is Fourier transformed to a Doppler velocity spectrum using the same algorithm as the real-time sensor processor (section 2). This signal is then processed in the same way as the POSS hardware (e.g., sampling rate, filters, FFT). The resultant POSS Doppler velocity spectrum gives the required modal parameters and other input variables used in MDA analysis.

This process is repeated for different habits, precipitation rates and wind speeds.

REFERENCES

American Meteorological Society, 2020: Hail. Glossary of Meteorology, http://glossary.ametsoc.org/wiki/Hail.

Böhm, H. P., 1989: A general equation for the terminal fall speed of solid hydrometeors. *J. Atmos. Sci.*, **46**, 2419–2427, https://doi.org/10.1175/1520-0469(1989)046<2419:AGEFTT>2.0.CO;2.

Brandes, E. A., G. Zhang, and J. Vivekanandan, 2002: Experiments in rainfall estimation with a polarimetric radar in a subtropical environment. *J. Appl. Meteor.*, **41**, 674–685, https://doi.org/10.1175/1520-0450(2002)041<0674:EIREWA>2.0.CO;2.

Bringi, V. N., P. C. Kennedy, G. Huang, C. Kleinkort, M. Thurai, and B. M. Notaroš, 2017: Dual-polarized radar and surface observations of a winter graupel shower with negative Z_{dr} column. *J. Appl. Meteor. Climatol.*, **56**, 455–470, https://doi.org/10.1175/JAMC-D-16-0197.1.

Campos, E., and I. Zawadzki, 2000: Instrumental uncertainties in *Z–R* relations. *J. Appl. Meteor.*, **39**, 1088–1102, https://doi.org/10.1175/1520-0450(2000)039<1088:IUIZRR>2.0.CO;2.

Chang, W.-Y., G. Lee, B. J.-D. Jou, W.-C. Lee, P.-L. Lin, and C.-K. Yu, 2020: Uncertainty in measured raindrop size distributions from four types of collocated instruments. *Remote Sens.*, **12**, 1167, https://doi.org/10.3390/rs12071167.

Cheng, L., and M. English, 1983: A relationship between hailstone concentration and size. *J. Atmos. Sci.*, **40**, 204–213, https://doi.org/10.1175/1520-0469(1983)040<0204:ARBHCA>2.0.CO;2.

——, ——, and R. Wong, 1985: Hailstone size distributions and their relationship to storm thermodynamics. *J. Climate Appl. Meteor.*, **24**, 1059–1067, https://doi.org/10.1175/1520-0450(1985)024<1059:HSDATR>2.0.CO;2.

Draine, B. T., and P. J. Flatau, 1994: Discrete-dipole approximation for scattering calculations. *J. Opt. Soc. Amer. A Opt. Image Sci. Vis.*, **11**, 1491–1499, https://doi.org/10.1364/JOSAA.11.001491.

——, and ——, 2013: User guide for the discrete dipole approximation code DDSCAT 7.3. arXiv, https://arxiv.org/abs/1305.6497.

Erfani, E., and D. L. Mitchell, 2017: Growth of ice particle mass and projected area during riming. *Atmos. Chem. Phys.*, **17**, 1241–1257, https://doi.org/10.5194/acp-17-1241-2017.

Fontaine, E., A. Schwarzenboeck, J. Delanoë, W. Wobrock, D. Leroy, R. Dupuy, C. Gourbeyre, and A. Protat, 2014: Constraining mass–diameter relations from hydrometeor images and cloud radar reflectivities in tropical continental and oceanic convective anvils. *Atmos. Chem. Phys.*, **14**, 11 367–11 392, https://doi.org/10.5194/acp-14-11367-2014.

Foote, G. B., and P. S. Du Toit, 1969: Terminal velocity of raindrops aloft. *J. Appl. Meteor.*, **8**, 249–253, https://doi.org/10.1175/1520-0450(1969)008<0249:TVORA>2.0.CO;2.

Garrett, T. J., C. Fallgatter, K. Shkurko, and D. Howlett, 2012: Fall speed measurement and high-resolution multi-angle photography of hydrometeors in free fall. *Atmos. Meas. Tech.*, **5**, 2625–2633, https://doi.org/10.5194/amt-5-2625-2012.

Gunn, K. L. S., and T. W. R. East, 1954: The microwave properties of precipitation particles. *Quart. J. Roy. Meteor. Soc.*, **80**, 522–545, https://doi.org/10.1002/qj.49708034603.

Herzegh, P. H., and A. R. Jameson, 1992: Observing precipitation through dual-polarization radar measurements. *Bull. Amer. Meteor. Soc.*, **73**, 1365–1376, https://doi.org/10.1175/1520-0477(1992)073<1365:OPTDPR>2.0.CO;2.

Heymsfield, A. J., and M. Kajikawa, 1987: An improved approach to calculating terminal velocities of plate-like crystals and graupel. *J. Atmos. Sci.*, **44**, 1088–1099, https://doi.org/10.1175/1520-0469(1987)044<1088:AIATCT>2.0.CO;2.

——, and C. D. Westbrook, 2010: Advances in the estimation of ice particle fall speeds using laboratory and field measurements. *J. Atmos. Sci.*, **67**, 2469–2482, https://doi.org/10.1175/2010JAS3379.1.

——, and R. Wright, 2014: Graupel and hail terminal velocities: Does a "supercritical" Reynolds number apply? *J. Atmos. Sci.*, **71**, 3392–3403, https://doi.org/10.1175/JAS-D-14-0034.1.

Huang, G., V. N. Bringi, D. Moisseev, W. A. Petersen, L. Bliven, and D. Hudak, 2015: Use of 2D-video disdrometer to derive mean density–size and Z_e–SR relations: Four snow cases from the light precipitation validation experiment. *Atmos. Res.*, **153**, 34–48, https://doi.org/10.1016/j.atmosres.2014.07.013.

IMSL, 2018: IMSL numerical libraries—Fortran 7.1 documentation. Rogue Wave Software, Inc., https://docs.roguewave.com/en/imsl/fortran.

ISO, 1975: Standard atmosphere. ISO Doc. 2533-1975, 108 pp., https://www.iso.org/standard/7472.html.

Junyent, F., V. Chandrasekar, V. N. Bringi, S. A. Rutledge, P. C. Kennedy, D. Brunkow, J. George, and R. Bowie, 2015: Transformation of the CSU–CHILL radar facility to a dual-frequency, dual-polarization Doppler system. *Bull. Amer. Meteor. Soc.*, **96**, 975–996, https://doi.org/10.1175/BAMS-D-13-00150.1.

Kajikawa, M., 1972: Measurement of falling velocity of individual snow crystals. *J. Meteor. Soc. Japan*, **50**, 577–584, https://doi.org/10.2151/jmsj1965.50.6_577.

Kennedy, P., M. Thurai, C. Praz, V. N. Bringi, A. Berne, and B. M. Notaroš, 2018: Variations in snow crystal riming and Z_{DR}: A case analysis. *J. Appl. Meteor. Climatol.*, **57**, 695–707, https://doi.org/10.1175/JAMC-D-17-0068.1.

Khvorostyanov, V. I., and J. A. Curry, 2005: Fall velocities of hydrometeors in the atmosphere: Refinements to a continuous analytical power law. *J. Atmos. Sci.*, **62**, 4343–4357, https://doi.org/10.1175/JAS3622.1.

Locatelli, J. D., and P. V. Hobbs, 1974: Fall speeds and masses of solid precipitation particles. *J. Geophys. Res.*, **79**, 2185–2197, https://doi.org/10.1029/JC079i015p02185.

Marshall, J. S., and W. M. Palmer, 1948: The distribution of raindrops with size. *J. Meteor.*, **5**, 165–166, https://doi.org/10.1175/1520-0469(1948)005<0165:TDORWS>2.0.CO;2.

Mishchenko, M. I., 2000: Calculation of the amplitude matrix for a nonspherical particle in a fixed orientation. *Appl. Opt.*, **39**, 1026–1031, https://doi.org/10.1364/AO.39.001026.

Mitchell, D. L., 1996: Use of mass- and area-dimensional power laws for determining precipitation particle terminal velocities. *J. Atmos. Sci.*, **53**, 1710–1723, https://doi.org/10.1175/1520-0469(1996)053<1710:UOMAAD>2.0.CO;2.

——, and A. J. Heymsfield, 2005: Refinements in the treatment of ice particle terminal velocities, highlighting aggregates. *J. Atmos. Sci.*, **62**, 1637–1644, https://doi.org/10.1175/JAS3413.1.

Mätzler, C., 2006: Dielectric properties of natural media. *Thermal Microwave Radiation: Applications for Remote Sensing*, Institution of Engineering and Technology, 427–506.

Nagumo, N., and Y. Fujiyoshi, 2015: Microphysical properties of slow-falling and fast-falling ice pellets formed by freezing associated with evaporative cooling. *Mon. Wea. Rev.*, **143**, 4376–4392, https://doi.org/10.1175/MWR-D-15-0054.1.

Notaroš, B., and Coauthors, 2016: Accurate characterization of winter precipitation using Multi-Angle Snowflake Camera, visual hull, advanced scattering methods and polarimetric radar. *Atmosphere*, **7**, 81, https://doi.org/10.3390/atmos7060081.

Pettersen, C., R. Bennartz, A. J. Merrelli, M. D. Shupe, D. D. Turner, and V. P. Walden, 2018: Precipitation regimes over central Greenland inferred from 5 years of ICECAPS observations. *Atmos. Chem. Phys.*, **18**, 4715–4735, https://doi.org/10.5194/acp-18-4715-2018.

Petty, G. W., and W. Huang, 2010: Microwave backscatter and extinction by soft ice spheres and complex snow aggregates. *J. Atmos. Sci.*, **67**, 769–787, https://doi.org/10.1175/2009JAS3146.1.

Ray, P. S., 1972: Broadband complex refractive indices of ice and water. *Appl. Opt.*, **11**, 1836–1844, https://doi.org/10.1364/AO.11.001836.

Sekhon, R. S., and R. C. Srivastava, 1970: Snow size spectra and radar reflectivity. *J. Atmos. Sci.*, **27**, 299–307, https://doi.org/10.1175/1520-0469(1970)027<0299:SSSARR>2.0.CO;2.

Sheppard, B. E., 1990: Measurement of raindrop size distributions using a small Doppler radar. *J. Atmos. Oceanic Technol.*, **7**, 255–268, https://doi.org/10.1175/1520-0426(1990)007<0255:MORSDU>2.0.CO;2.

——, 2007: Sampling errors in the measurement of rainfall parameters using the Precipitation Occurrence Sensor System (POSS). *J. Atmos. Oceanic Technol.*, **24**, 125–140, https://doi.org/10.1175/JTECH1956.1.

——, and P. I. Joe, 2008: Performance of the precipitation occurrence sensor system as a precipitation gauge. *J. Atmos. Oceanic Technol.*, **25**, 196–212, https://doi.org/10.1175/2007JTECHA957.1.

Shivola, A. H., 1989: Self-consistency aspects of dielectric mixing theories. *IEEE Trans. Geosci. Remote Sens.*, **27**, 403–415, https://doi.org/10.1109/36.29560.

Skofronick-Jackson, G., and Coauthors, 2015: Global Precipitation Measurement Cold Season Precipitation Experiment (GCPEX): For measurement's sake, let it snow. *Bull. Amer. Meteor. Soc.*, **96**, 1719–1741, https://doi.org/10.1175/BAMS-D-13-00262.1.

Szyrmer, W., and I. Zawadzki, 2010: Snow studies. Part II: Average relationship between mass of snowflakes and their terminal fall velocity. *J. Atmos. Sci.*, **67**, 3319–3335, https://doi.org/10.1175/2010JAS3390.1.

Thurai, M., G. J. Huang, V. N. Bringi, W. L. Randeu, and M. Schönhuber, 2007: Drop shapes, model comparisons, and calculations of polarimetric radar parameters in rain. *J. Atmos. Oceanic Technol.*, **24**, 1019–1032, https://doi.org/10.1175/JTECH2051.1.

Ulbrich, C. W., 1983: Natural variations in the analytical form of the raindrop size distribution. *J. Climate Appl. Meteor.*, **22**, 1764–1775, https://doi.org/10.1175/1520-0450(1983)022<1764:NVITAF>2.0.CO;2.

Wilks, D. S., 1995: *Statistical Methods in the Atmospheric Sciences: An Introduction*. Academic Press, 467 pp.

WMO, 2018: Precipitation gauge errors and corrections. Guide to meteorological instruments and methods of observation, WMO Rep. WMO-8, 6.4, https://www.wmo.int/pages/prog/www/IMOP/CIMO-Guide.html.